

The X-ray Pulse Profile of BG CMi

Chul-Sung Choi

*International Center for Astrophysics, Korea Astronomy and Space Science
Institute, 36-1 Hwaam, Yusong, Daejeon 305-34, Korea*

Tadayasu Dotani

*Institute of Space and Astronautical Science, Japan Aerospace Exploration Agency,
3-1-1 Yoshinodai, Sagami-hara, Kanagawa 229-8510, Japan*

Yonggi Kim

University Observatory, Chungbuk National University, Cheongju 361-763, Korea

Dongsu Ryu^{*}

*Department of Astronomy and Space Science, Chungnam National University,
Daejeon 305-764, Korea*

Abstract

We present an analysis of the X-ray data of a magnetic cataclysmic variable, BG CMi, obtained with ROSAT in March 1992 and with ASCA in April 1996. We show that four peaks clearly exist in the X-ray pulse profile, unlike a single peak found in the optical profile. The fluxes of two major pulses are $\sim 2 - 5$ times larger than those of two minor pulses. The fraction of the total pulsed flux increases from 51% to 85% with increasing energy in $0.1 - 2.0$ keV, whereas it decreases from 96% to 22% in $0.8 - 10$ keV. We discuss the implications of our findings for the origin of the pulse profile and its energy dependence.

Key words:

cataclysmic variables : close binaries : individual stars (BG CMi) : X-ray binaries

^{*} Corresponding author.

Email addresses: cschoi@kasi.re.kr (Chul-Sung Choi),
dotani@astro.isas.jaxa.jp (Tadayasu Dotani), ykkim153@chungbuk.ac.kr
(Yonggi Kim), ryu@canopus.cnu.ac.kr (Dongsu Ryu).

1 Introduction

BG CMi is a magnetic cataclysmic variable (mCV), known as an intermediate polar (IP), with an orbital period of 3.235 hr (McHardy et al., 1984, for review of IPs, see, e.g., Patterson 1994). The primary star, exhibiting pulsations of fluxes in the X-ray, optical, and infrared bands, is a rotating magnetic white dwarf. Its magnetic field strength has been inferred to be $B = (2 - 6) \times 10^6$ G (Chanmugam et al., 1990), based on circular polarization observations in the optical and infrared bands (Penning, Schmidt, & Liebert, 1986; West, Berriman, & Schmidt, 1987). However, the fundamental properties of the secondary star are yet poorly known. The system parameters as well as the distance to the binary system are not well constrained.

In the optical band, a quasi-sinusoidal pulse profile was clearly seen at a period of 913.5 s, together with an orbital modulation of brightness over a period of 3.235 hr (e.g., De Martino et al., 1995; Kim et al., 2005). The optical studies claimed that the 913.5 s period is that of the white dwarf’s spin. According to the pulse period analysis, the primary is spinning up, but the rate seems to change in time (Kim et al., 2005, and reference therein). De Martino et al. (1995) found that the fraction of the pulsed flux in the optical band also varies with time and wavelength.

The pulsation and the orbital modulation were also detected in X-ray at the same periods (Terada, Ishida, & Makishima, 2004; Parker, Norton, & Mukai, 2005). However, the X-ray pulse profile is non-sinusoidal and hinted possibly multiple peaks. McHardy et al. (1987) reported that there are two emission components in the X-ray of a medium energy range, one being pulsed and radiated from the magnetic poles of the white dwarf and the other being unpulsed and radiated from the regions where accretion streams impact the magnetosphere. An iron $K\alpha$ fluorescence line was observed at ~ 6.4 keV with no significant variations over the pulse period (e.g., Norton et al., 1992; Ezuka & Ishida, 1999).

The study of this paper focuses on the X-ray pulse profile of BG CMi and its energy dependence from the ROSAT and ASCA archival data. Based on the analysis results, the geometry of X-ray emitting regions is discussed.

2 Observation and Data Reduction

BG CMi was observed with ROSAT on March 28 to 29, 1992 with on-source time of 8.4×10^3 s. It was observed twice with ASCA with an interval of 2 days: April 14 through 15, 1996 with on-source time of 3.7×10^4 s and April 17

through 18, 1996 with on-source time of 3.6×10^4 s (see also Ezuka & Ishida, 1999; Terada, Ishida, & Makishima, 2004; Parker, Norton, & Mukai, 2005).

The ROSAT observation was made with Position Sensitive Proportional Counter (PSPC-B) mounted on the focal plane of the X-ray telescope. The PSPC covers the energy range of 0.1 – 2 keV and has a relatively high spatial resolution of $\sim 25''$ at 1 keV over 2° diameter field of view. The PSPC is known to have a very high rejection efficiency of particle background events, 99.9%, with a typical count rate of 4×10^{-6} counts s^{-1} arcmin^{-2} keV^{-1} (Plucinsky et al., 1993). We acquired the screened data of BG CMi from the HEASARC public archives.

According to the second ROSAT source catalog of pointed observations with PSPC¹, other X-ray sources may be present within a circular region of radius 0.1° from BG CMi (see Table 1). For instance, an X-ray source which is relatively bright and has a count rate of 1.25×10^{-2} counts s^{-1} is located near BG CMi at the position of R.A. = 112.88126° and DEC. = 10.06978° (J2000) with an angular separation of $7.8'$. Caution therefore is needed in an analysis of X-ray data of BG CMi. Considering this situation, we restrict a source extraction region to a circle of radius $3'$ centered at the position of BG CMi.

ASCA is equipped with four thin-foil X-ray telescopes, focusing X-rays onto four focal plane detectors, of which two are Solid-state Imaging Spectrometers (SIS0 and SIS1) and two are Gas Imaging Spectrometers (GIS2 and GIS3). Each SIS consists of four CCD chips with an energy resolution of $\sim 50 - 160$ eV in the range of 0.4 – 10.0 keV, while GISs have an energy resolution of $\sim 200 - 600$ eV in 0.8 – 10.0 keV. The telescopes have a $\sim 3'$ half-power diameter of the point spread function (PSF), and the intrinsic PSF of GISs depends on the incident X-ray energy and is Gaussian with a FWHM of $0.5 \times \sqrt{5.9 \text{ keV}/E}$ arcmin (where E is the X-ray energy in keV).

The ASCA observations were made with both SISs and GISs. SISs were operated in the 2 CCD faint mode and GISs in the pulse-height (PH) mode. The time resolution of SISs in the 2 CCD mode is 8 s and that of GISs in the PH mode is 62.5/500 ms for high/medium telemetry bit rates. SISs in the 2 CCD mode provide a $11' \times 23'$ rectangular field of view, while GISs give a circular field of view with a diameter of $50'$, regardless of their observational mode.

We acquired raw ASCA data from public archives and applied ‘strict’ data screening criteria to the GIS and SIS data to reduce possible contaminations from the Earth’s bright limb and from the regions of high particle background. For example, the SIS data were rejected when the pointing direction of the

¹ <http://wave.xray.mpe.mpg.de/rosat/rra>

telescope is less than 40° from the Earth’s bright limb and the upper-threshold of the radiation belt monitor was set to 50. Hot and flickering pixels were removed from the SISs and a grade-based selection criterion was applied to the data. Other screening criteria were set to the recommended values (we checked difference in the GIS data by applying different screening criteria to the elevation angle, which is defined as the angle between the source and the Earth’s limb, e.g. 5° and 10° , but found no significant difference; we therefore applied the recommended value to the elevation angle). After this screening, the source events were extracted from the $3'$ radius region for both the GISs and SISs data.

3 Results

We extracted light curves after converting the X-ray arrival times to the barycentric times of the solar system. Therefore, all the dates or times described in this section are based on the Barycentric Dynamical Time (TDB). The extracted light curves have a time resolution of 0.1 s for the PSPC data, 0.5 s for the GISs, and 8.0 s for the SISs.

3.1 Pulse Period

To confirm the presence of pulses in the current X-ray data, we did a period search using an epoch folding method, e.g., ‘efsearch’ in FTOOLS (or XRONOS). For this work, we focused on the PSPC and GIS data that have a better time resolution than the SIS data. In this search, we did not correct the Doppler effect due to the binary motion, because it is negligible in the current data. Figure 1 shows the result obtained from the GIS data.

The best periods, which were determined by fitting a Gaussian function to the centroid of χ^2 -peak, are $P = 913.6 \pm 0.3$ s for the PSPC data and $P = 913.5 \pm 0.1$ s for the GIS data (where the errors in χ^2 are included). These periods are consistent with each other within the errors as well as with those reported in previous X-ray and optical studies. It is noted from the χ^2 -plot that there are higher harmonics of the period P and a beat between the orbital and pulse periods, marked with vertical short-dashed lines, suggesting that P is the fundamental period of the source and is the spin period of the white dwarf.

3.2 Pulse Profile

Figure 2 and Figure 3 show the mean pulse profiles (crosses) obtained from the ROSAT and ASCA data, respectively. The start and stop times of the data are indicated in each figure. The ROSAT data were folded at the period of 913.6 s from the epoch MJD 48709.28492 and the ASCA data were folded at the period of 913.5 s from the epoch MJD 50187.79824. The epochs for pulse phase zero were taken at the centers of the highest pulses (RP1 and AP2), which were determined independently for the ROSAT and ASCA data through model fits to the profiles (see below). For this we included the SIS data to increase the data statistics. (Before we included the SIS data, we inspected visually the pulse profiles of the four ASCA instruments. We found no significant difference in, e.g., overall profile, peak positions, and relative pulse height.)

As displayed in Figure 2, the ROSAT data in the 0.1 – 2.0 keV range exhibit two peaks (or pulses), labeled ‘RP1’ and ‘RP2’, over one cycle of the pulse profile. The two pulses are not separated by 0.5 in phase and their heights are not equal. Furthermore, the widths seem to be different too. The profile can be approximated by a model of two Gaussians on the top of a constant base, as represented with the solid curve. On the other hand, the ASCA data in the 0.8 – 10.0 keV range exhibit four pulses labeled ‘AP1’ – ‘AP4’ in Figure 3, and the profile is reproducible by a model of four Gaussians on the top of a constant base (see the following subsection for the model function; we checked whether the profile can be fitted with other models, e.g., sine plus two Gaussians, but found that none reproduces the profile successfully). From the figure, it is noted that the AP1 and AP3 pulses are separated by ~ 0.5 in phase and the AP2 and AP4 pulses are separated also by ~ 0.5 . However, the overall profiles of AP1/AP3 and AP2/AP4 are different to each other. The difference in the ROSAT and ASCA profiles will be described in details in the following subsection.

In order to identify which pulse is coincident with the optical pulse maximum, we calculated the epoch that is near the start time of the X-ray data, using the recently presented ephemerides by, e.g., Kim et al. (2005)², Hellier (1997), and Pych et al. (1996). The vertical short-dashed lines in Figures 2 and 3 represent the optical pulse maxima calculated from the ephemerides. For the lines we did not correct the difference between the heliocentric time and the TDB because the difference is negligibly small ($\lesssim 3$ s) compared to the pulse

² They presented in the abstract a fourth-order polynomial ephemeris which is statistically optimal for the optical pulse minimum. However, the ephemeris should be for the pulse maximum, otherwise it becomes inconsistent with the observed ephemeris presented in their paper by a half phase.

period. Taking into account of the uncertainties in the optical ephemerides, $\sim 0.02 - 0.03$ in phase, we conclude that RP1 and AP2 correspond to the optical pulse maximum. In what follows, we consider that the pulse phases, originally determined independently for the ROSAT and ASCA data, are in fact coherently connected with each other.

3.3 Energy-Resolved Pulse Profiles

To understand the difference in the ROSAT and ASCA profiles and also to see how the profiles vary with energy, we examine the energy-resolved pulse profiles obtained in the four different energy bands, $0.1 - 0.8$ keV, $0.8 - 2.0$ keV, $2.0 - 4.0$ keV, and $4.0 - 10$ keV. Figure 4 shows the profiles, where the ROSAT and ASCA data were folded independently using the epochs and periods described in the previous subsection. The backgrounds were not subtracted from the pulse profiles of Figure 4, because it was difficult to acquire the appropriate background data from the nearby annular region due to the presence of contamination sources. However, we note that the backgrounds are generally small compared to the unpulsed fluxes in Table 2 as estimated below.

The typical fluxes of a blank sky observed with ASCA GIS2 are 1.3×10^{-3} counts s^{-1} in $0.8 - 2.0$ keV, 1.1×10^{-3} counts s^{-1} in $2.0 - 4.0$ keV, and 5.1×10^{-3} counts s^{-1} in $4.0 - 10$ keV for the same size as the source extraction region in the data of cutoff rigidity greater than 4 GeV/c. The SIS0 data show the fluxes of 3.4×10^{-3} counts s^{-1} in $0.8 - 2.0$ keV, 1.5×10^{-3} counts s^{-1} in $2.0 - 4.0$ keV, and 1.7×10^{-3} counts s^{-1} in $4.0 - 10$ keV for the same size as the source extraction region in the data of cutoff rigidity greater than 6 GeV/c. Because BG CMi is located far from the galactic plane, we ignored the contribution from the galactic ridge emission (e.g., Kaneda et al., 1997). These mean fluxes of a blank sky are much smaller than the unpulsed fluxes of the ASCA data in $2.0 - 10$ keV (Table 2). However, they are significant in $0.8 - 2.0$ keV. This means that we need to be careful in interpreting the unpulsed flux of the ASCA data in this lowest energy band. According to the ROSAT PSPC all-sky survey, the flux of the diffuse X-ray background can be roughly estimated to $\sim 10^{-4}$ counts s^{-1} arcmin $^{-2}$ in $0.1 - 2.0$ keV (Snowden et al., 1995). It is much smaller than the unpulsed fluxes of the ROSAT data (Table 2), even if we consider the size of the event extraction region. We note that the contribution of nearby contamination sources is also small compared to the unpulsed flux in the ROSAT band. Therefore, below we argue that the energy-dependent behavior of the pulse fraction³ as well as the presence of the unpulsed fluxes are intrinsic to the source.

³ Defined as the ratio of the flux in pulses to the total (pulsed + unpulsed) flux.

To study the pulse parameters quantitatively we chose a model of two or four Gaussians on the top of a constant base, as follows;

$$f(x) = C + \sum_{i=1}^{2 \text{ or } 4} N_i \exp[-(x - P_i)^2/2W_i^2], \quad (1)$$

where $f(x)$ is the folded pulse profile, x is the phase, P is the Gaussian center, W is the width, N is the height, and C is a constant that represents the unpulsed flux level. In this model, all the parameters were allowed to be fitted. The parameters of the best-fit model, represented as solid and short-dashed curves in Figure 4, are summarized in Table 2. The mean pulsed flux in each profile is also calculated in the table using the best-fit parameters.

Although the ROSAT and ASCA data were obtained with an interval of 4 years, their pulse profiles are surprisingly similar. This means that BG CMI showed very little time variation in 4 years. One may claim that the pulse profiles in the common energy band of 0.8 - 2.0 keV look different in the ROSAT and ASCA data (we checked the ROSAT profile by applying a different folding period, e.g., 913.5 s, but found no significant difference). That is, in the ROSAT data of Figure 4b, the two pulses that correspond to AP1 & AP4 in the ASCA data of Figure 4c seem to be absent. We attribute the difference to the different energy responses of ROSAT PSPC and ASCA SIS/GIS. PSPC has a larger effective area for softer X-rays in this energy band, whereas SIS/GIS has a larger effective area for harder X-rays. In fact, if we check carefully the parameters in Table 2, there is a hint of AP1 & AP4 in the ROSAT profile. For example, the width of RP1 is almost identical to the width of AP2, whereas the width of RP2 is larger than that of AP3. This broader pulse may be interpreted as a superposition of two pulses AP3 and AP4 of the ASCA profile. In addition, the possible existence of a broad hump above the unpulsed level, which appears at the phase range $\sim 0.5 - 0.8$ in Figure 4a, may support this interpretation. Although we claim the similarity in the pulse profiles of ROSAT and ASCA, it needs to be confirmed again through observations covering a wide energy range of 0.1 - 10 keV.

By analyzing the energy-resolved pulse profiles together with the fit parameters in Table 2, we obtained the following results:

- (1) The separation of the AP2 and AP4 pulses, from peak to peak, is sustained to be consistent, ~ 0.5 in phase, irrespective of energy band. The AP1 and AP3 pulses are basically separated by ~ 0.5 , but the separation tends to increase with increasing X-ray energy.
- (2) The pulse widths for RP1 and AP2 increase clearly with increasing energy, from 0.04 to 0.11 in phase.
- (3) The pulsed fluxes for AP2 and AP3 (major pulses) are $\sim 2 - 5$ times larger than the fluxes for AP1 and AP4 (minor pulses) at all energies.

The flux ratios tend to be lower at higher X-ray energy. The tendency explains the profile change in the ASCA data, seen in Figure 4c through Figure 4e.

- (4) The total pulse fraction decreases with increasing energy, from 96% to 22% in the energy range of 0.8 – 10.0 keV.⁴ On the other hand, the pulse fraction in RP1 and RP2 increases from 51% to 85% with increasing energy in the energy range of 0.1 – 2.0 keV. These energy-dependent behavior is mainly associated with the flux variation of the unpulsed component.

4 Discussion

4.1 Pulse Profile

As shown in §3.2, multiple X-ray pulses exist consistently in 0.1 – 10 keV with relatively narrow widths and show no significant phase shift over the selected energy bands. These facts suggest that the pulsed radiation originates from restricted regions of the rotating compact object. The pulse profile in the ASCA data of 0.8 – 10 keV in Figure 4 contains four pulses, which are particularly well separated in the lower energy band of 0.8 – 2.0 keV. The ROSAT data in 0.1 – 2.0 keV also indicate possibly four pulses. The four pulse profile requires in general four X-ray emitting regions on the surface of the white dwarf, if all the pulses are considered to come from a single object. In this sense, the postulate that a multipole geometry of magnetic field exists in the primary star can not be excluded completely (see e.g., Beuermann et al., 2007).

Nevertheless, if the primary star should have a dipole magnetic field geometry, two pulses need to be generated from a single magnetic pole. Then we argue that the major pulses (AP2 & AP3) should be produced from one magnetic pole, and the minor pulses (AP1 & AP4) from the opposite pole, based on the following reasons: A dipole magnetic field generally produces two pulses separated by ~ 0.5 in phase, unless the dipole moment is severely distorted. We note that the AP1 and AP3 pulses are separated by ~ 0.5 in phase and the AP2 and AP4 pulses are also separated by ~ 0.5 in phase. Furthermore, if two pulses are produced by a single pole, they would have a similar amplitude, because the amplitude is determined in principle by the geometric effect, such as the occultation of the emitting region. However, the existence of deep troughs between the major pulses and between the minor pulses in

⁴ When we calculated the pulse fraction, we subtracted the backgrounds obtained from the blank sky observation data.

Figure 4 implies that the two emission regions in a pole should be well separated. Such separation favors large magnetic pole areas (or polar caps), unlike the conventional dipole field geometry of mCVs that has two small-size polar caps (see e.g., Rosen, Mason, & Cordova, 1988). One interesting point is that the large polar cap hypothesis is also required to explain the observations of circular polarization in BG CMi (e.g., West, Berriman, & Schmidt, 1987; Chanmugam et al., 1990).

4.2 *Energy Dependence of Pulse Fraction*

The total pulse fraction decreases clearly from 96% to 22% with increasing X-ray energy in 0.8 – 10.0 keV (§3.3). It is also worthwhile to mention that the pulse width decreases from 0.11 to 0.04 in phase with decreasing energy in RP1 and AP2. The energy dependence of the pulse fraction may reflect the temperature distribution in the X-ray emitting regions. That is, if a relatively hot plasma is formed at a large height above the magnetic poles, the plasma may be little occulted by the white dwarf and will contribute largely to the unpulsed X-ray flux. On the other hand, if a relatively cool plasma is located just above the magnetic poles, it may be occulted largely by the white dwarf and will contribute much to the pulsed X-ray flux. We therefore conjecture that the magnetically channeled accreting matter cools down by radiative cooling processes while it travels toward the magnetic pole areas. This idea may also explain the energy dependence of the pulse width, if we consider a finite opening angle of the magnetic field. We leave this issue as a future study because the signal to noise ratios of the spectral data are not good enough to test the idea.

4.3 *Optical Profile*

It is interesting to note that the optical profile has a single, quasi-sinusoidal pulse, unlike the X-ray profile we studied. The total pulse fraction in optical is relatively low, $\lesssim 30\%$, and varies with wavelength (De Martino et al., 1995). The low pulse fraction as well as the quasi-sinusoidal profile suggest that the pulsed flux originates from a relatively large area which is occulted partly and periodically by the rotating white dwarf.

As we showed in §3.2, the expected optical pulse maximum matches well with the RP1 and AP2 pulses. Likewise, the fact that the pulsed flux of the major pulses is larger by ~ 5 times than the flux of the minor pulses indicates that there exists an appropriate geometrical condition for producing the quasi-sinusoidal profile. Therefore, the pulsed flux in the optical band may be suggested to come from the pole area that was heated up by the illumination of

the X-rays emanating from the channeled accreting matter. Alternatively, the pulsed flux may originate from the matter that is cooling and spreading over the white dwarf surface after it settled on the polar region as discussed by Choi & Yi (2000).

5 Summary

Our findings are summarized as follows:

- (1) BG CMi has an X-ray profile with four pulses over the period of 913.5 s.
- (2) The fluxes of the major pulses AP2 and AP3 are $\sim 2 - 5$ times larger than those of the minor pulses AP1 and AP4.
- (3) The pulse fraction increases from 51% to 85% with increasing energy in $0.1 - 2.0$ keV, whereas it decreases from 96% to 22% in $0.8 - 10$ keV.
- (4) Unlike the X-ray profile, the optical profile has single, quasi-sinusoidal pulse. Among the four X-ray pulses, the highest one coincides with the optical pulse maximum.

Acknowledgements

C.S.C. and Y.G.K. thank Dr. I. Andronov for comments and discussions on results of this work. C.S.C. thanks Dr. H. Kim for discussions of magnetic field configurations in compact stars. This work was supported in part by the Korea Science & Engineering Foundation through the grant of the basic research program R01-2004-000-1005-0. The work of D.R. was also supported in part by Korea Foundation for International Cooperation of Science & Technology (KICOS) through the Cavendish-KAIST Research Cooperation Center.

References

- Beuermann, K., Euchner, F., Reinsch, K., Jordan, S., & Gansicke, B. T. 2007, *A&A*, 463, 647
- Chanmugam, G., Frank, J., King, A. R., & Lasota, J.-P. 1990, *ApJ*, 350, L13
- Choi, C. S., & Yi, I. 2000, *ApJ*, 538, 862
- De Martino, D., Mouchet, M., Bonnet-Bidaud, J. M., Vio, R., Rosen, S. R., Mukai, K., Augusteijn, T., & Garlick, M. A. 1995, *A&A*, 298, 849
- Ezuka, H., & Ishida, M. 1999, *ApJS*, 120, 277
- Hellier, C. 1997, *MNRAS*, 288, 817

- Kaneda, H., Makishima, K., Yamauchi, S., Koyama, K., Matsuzaki, K., & Yamasaki, N. Y. 1997, *ApJ*, 491, 638
- Kim, Y. G., Andronov, I. L., Park, S. S., & Jeon, Y.-B. 2005, *A&A*, 441, 663
- McHardy, I. M., Pye, J. P., Fairall, A. P., & Menzies, J. W. 1987, *MNRAS*, 225, 355
- McHardy, I. M., Pye, J. P., Fairall, A. P., Warner, B., Cropper, M., & Allen, S. 1984, *MNRAS*, 210, 663
- Norton, A. J., McHardy, I. M., Lehto, H. J., & Watson, M. G. 1992, *MNRAS*, 258, 697
- Parker, T. L., Norton, A. J., & Mukai, K. 2005, *A&A*, 439, 213
- Patterson, J. 1994, *PASP*, 106, 209
- Penning, W. R., Schmidt, G. D., & Liebert, J. 1986, *ApJ*, 301, 881
- Plucinsky, P. P., Snowden, S. L., Briel, U. G., Hasinger, G., & Pfeffermann, E. 1993, *ApJ*, 418, 519
- Pych, W., Semeniuk, I., Olech, A., & Ruszkowski, M. 1996, *Acta Astronomica*, 46, 279
- Rosen, S. R., Mason, K. O., & Cordova, F. A. 1988, *MNRAS*, 231, 549
- Snowden, S. L., Freyberg, M. J., Plucinsky, P. P., Schmitt, J. H. M., Trumper, J., Voges, W., Edgar, R. J., McCammon, D., & Sanders, W. T. 1995, *ApJ*, 454, 643
- Terada, Y., Ishida, M., & Makishima, K. 2004, *PASJ*, 56, 533
- West, S. C., Berriman, G., & Schmidt, G. D. 1987, *ApJ*, 322, L35

Table 1

Possible Cataloged X-ray Sources near BG CMi^a

Source Name	R.A. ^b	DEC. ^b	Count Rate (counts s ⁻¹)
2RXP J073138.1+100108	112.90876	10.01917	$(9.4 \pm 3.7) \times 10^{-4}$
2RXP J073126.8+095959	112.86167	9.99972	$(1.0 \pm 0.4) \times 10^{-3}$
2RXP J073148.2+095810	112.95084	9.96945	$(1.1 \pm 0.4) \times 10^{-3}$
BG CMi	112.87084	9.94028	$(8.7 \pm 0.3) \times 10^{-2}$
2RXP J073151.3+095430	112.96375	9.90833	$(2.0 \pm 0.6) \times 10^{-3}$

^aWithin a circular region of radius 0.1° which is centered at BG CMi.^bEquatorial coordinates are in equinox J2000.

Table 2

Best-Fit Pulse Parameters and Calculated Pulsed fluxes

Pulse or Peak	Energy Band			
	0.1 – 0.8 keV	0.8 – 2.0 keV	2.0 – 4.0 keV	4.0 – 10 keV
RP1				
P (phase)	$0.995^{+0.005}_{-0.006}$	$1.00^{+0.02}_{-0.01}$
W (phase)	$0.036^{+0.005}_{-0.006}$	$0.065^{+0.010}_{-0.010}$
$Flux^{*1}$ (10^{-3} counts s^{-1})	$21.5^{+8.3}_{-6.4}$	$18.3^{+7.1}_{-5.5}$
RP2				
P (phase)	$1.27^{+0.01}_{-0.01}$	$1.28^{+0.02}_{-0.02}$
W (phase)	$0.06^{+0.01}_{-0.01}$	$0.10^{+0.02}_{-0.02}$
$Flux^{*1}$ (10^{-3} counts s^{-1})	$15.0^{+7.1}_{-5.3}$	$17.7^{+9.1}_{-6.3}$
C^{*2} (10^{-3} counts s^{-1})	34.9	6.4
AP1				
P (phase)	...	$0.77^{+0.01}_{-0.01}$	$0.76^{+0.01}_{-0.01}$	$0.76^{+0.02}_{-0.02}$
W (phase)	...	$0.067^{+0.013}_{-0.010}$	$0.055^{+0.010}_{-0.007}$	$0.06^{+0.02}_{-0.02}$
$Flux^{*1}$ (10^{-3} counts s^{-1})	...	$1.6^{+0.6}_{-0.4}$	$3.6^{+0.9}_{-0.8}$	$2.4^{+1.7}_{-1.0}$
AP2				
P (phase)	...	$1.016^{+0.004}_{-0.005}$	$1.009^{+0.007}_{-0.008}$	$1.01^{+0.02}_{-0.02}$
W (phase)	...	$0.068^{+0.006}_{-0.006}$	$0.088^{+0.010}_{-0.009}$	$0.11^{+0.03}_{-0.03}$
$Flux^{*1}$ (10^{-3} counts s^{-1})	...	$5.2^{+0.8}_{-0.8}$	$10.5^{+1.9}_{-1.7}$	$6.1^{+3.3}_{-2.0}$
AP3				
P (phase)	...	$1.282^{+0.003}_{-0.013}$	$1.32^{+0.03}_{-0.04}$	$1.36^{+0.02}_{-0.04}$
W (phase)	...	$0.075^{+0.012}_{-0.017}$	$0.09^{+0.02}_{-0.02}$	$0.09^{+0.02}_{-0.03}$
$Flux^{*1}$ (10^{-3} counts s^{-1})	...	$4.8^{+1.0}_{-2.5}$	$9.8^{+3.3}_{-3.6}$	$5.3^{+2.4}_{-2.6}$
AP4				
P (phase)	...	$1.50^{+0.04}_{-0.16}$	$1.49^{+0.02}_{-0.03}$	1.50^{*3}
W (phase)	...	$0.10^{+0.10}_{-0.03}$	$0.06^{+0.02}_{-0.03}$	0.036^{*3}
$Flux^{*1}$ (10^{-3} counts s^{-1})	...	$1.7^{+2.3}_{-0.7}$	$2.3^{+2.9}_{-0.4}$	0.7
C^{*2} (10^{-3} counts s^{-1})	...	2.8	20.5	52.4

Note - Models of two or four Gaussians on the top of a constant base were fitted to the pulse profiles. The full-width at half-maximum can be obtained by multiplying a constant, i.e., $W_{FWHM} = 2.354 \times W$. All the attached errors are at 90% confidence level.

^{*1}The mean pulsed flux for each pulse was calculated using the best-fit parameters.

^{*2}A constant that represents the unpulsed flux level.

^{*3}Fixed in the fit.

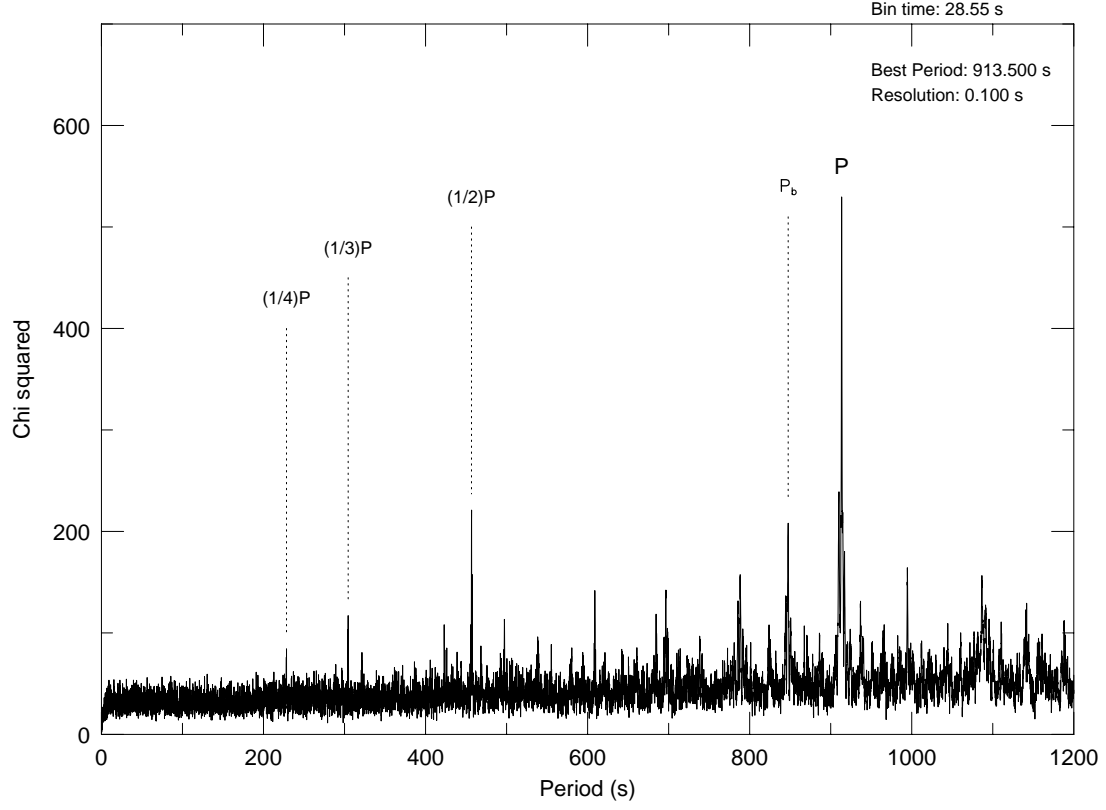


Fig. 1. χ^2 -plot as a function of trial period for the GIS data in the entire energy range. The harmonics of the period P , labeled with $\frac{1}{2}P$ (456.7 s), $\frac{1}{3}P$ (304.5 s), and $\frac{1}{4}P$ (228.4 s), are clearly seen in the figure. The peak labeled with P_b ($\equiv \frac{P_{\text{orb}}P}{P_{\text{orb}}+P} = 847.5$ s) is the beat between orbital (3.235 hr) and pulse (913.5 s) periods.

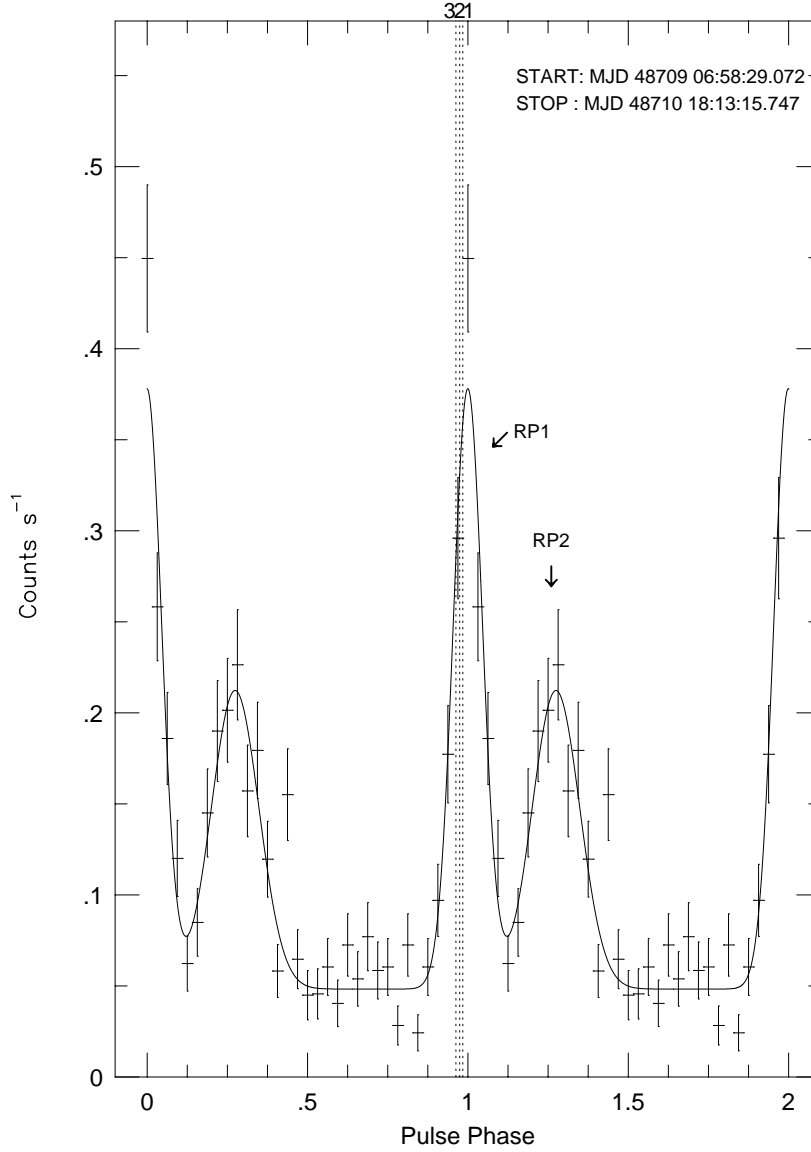


Fig. 2. Pulse profile of the ROSAT data folded at period 913.6 s from the epoch MJD 48709.28492. The pulse phase has been repeated over two cycles. A model of two Gaussians on the top of a constant base (solid curve) was fitted to the profile (crosses) from the minimum to the minimum. The vertical short-dashed lines represent the optical pulse maximum expected from the recent ephemerides: the number 1 at the top of the figure is from Kim et al. (2005), 2 is from Pych et al. (1996), and 3 is from Hellier (1997).

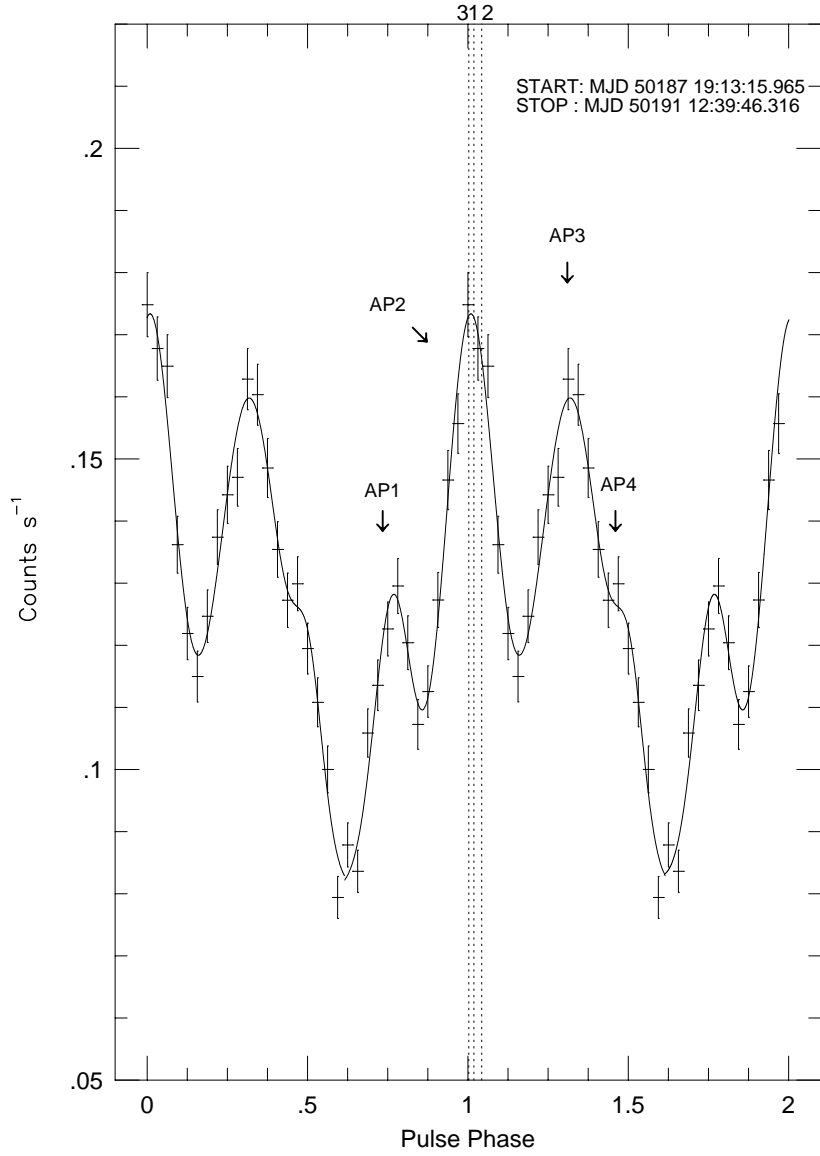


Fig. 3. Pulse profile of the ASCA data folded at period 913.5 s from the epoch MJD 50187.79824. The count rate is an average value detected by GISs and SISs. A model of four Gaussians on the top of a constant base (solid curve) was fitted to the profile (crosses) from the minimum to the minimum. The vertical short-dashed lines are the same as in Figure 2.

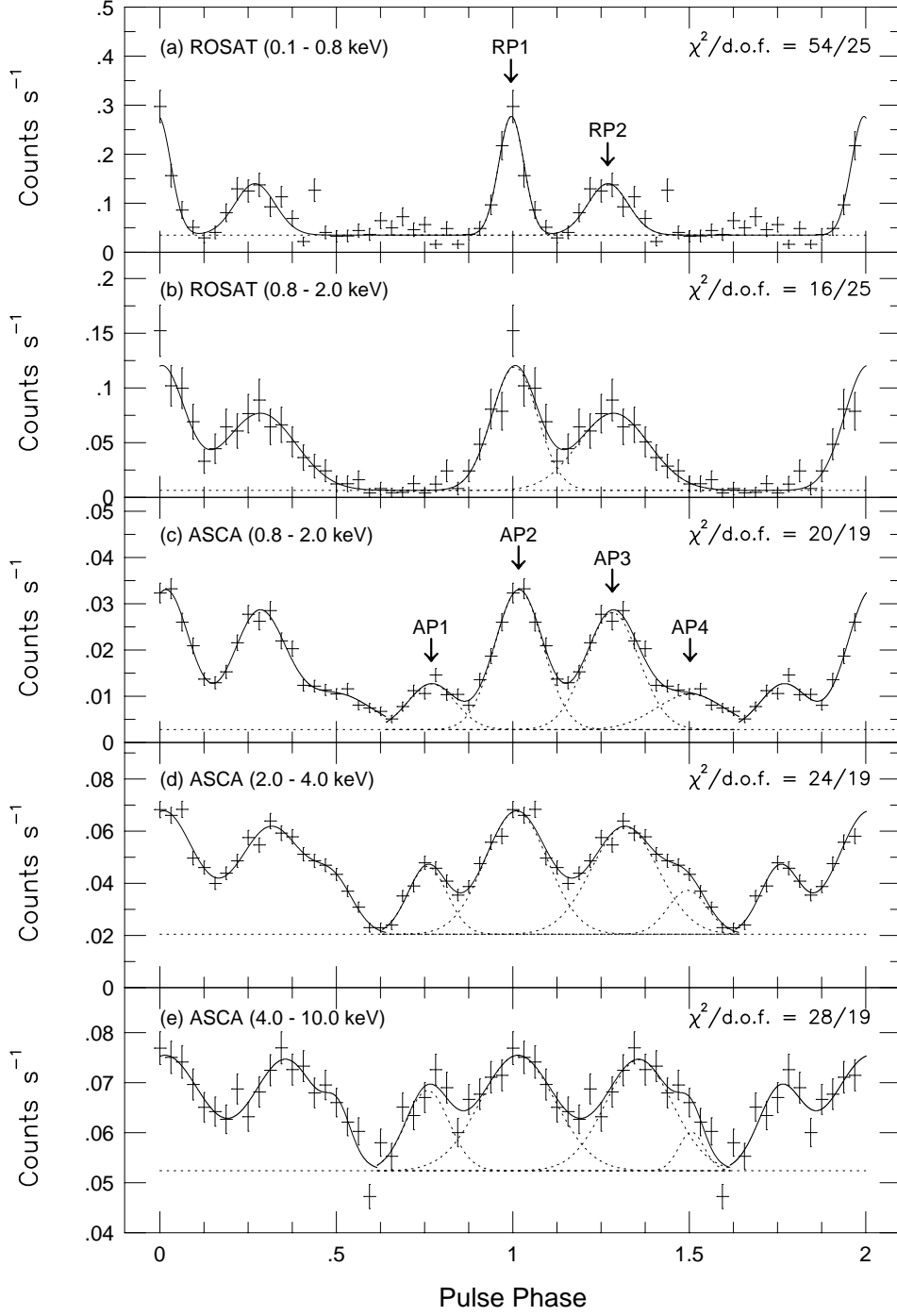


Fig. 4. Energy-resolved pulse profiles of BG CMi. The folding epoch and period for the ROSAT and ASCA data are the same as in Figures 2 and 3, respectively. The short-dashed curves and horizontal lines represent each Gaussian component and the unpulsed flux level, respectively. Goodness of the model-fit is inserted in each figure. The count rate in (c) through (e) is an average value detected by GISs and SISs.